The Astrophysical Journal Letters, 935:L14 (11pp), 2022 August 10 https://doi.org/10.3847/2041-8213/ac85af


# Tracking the Ice Mantle History in the Solar-type Protostars of NGC 1333 IRAS 4

Marta De Simone[1,2], Cecilia Ceccarelli[1], Claudio Codella[1,2], Brian E. Svoboda[3], Claire J. Chandler[3], Mathilde Bouvier[1], Satoshi Yamamoto[4], Nami Sakai[5], Yao-Lun Yang[5,6], Paola Caselli[7], Bertrand Lefloch[1], Hauyu Baobab Liu[8], Ana López-Sepulcre[1,9], Laurent Loinard[10], Jaime E. Pineda[7], and Leonardo Testi[2,11,12]
[1] Univ. Grenoble Alpes, CNRS, IPAG, F-38000 Grenoble, France; marta.desimone@univ-grenoble-alpes.fr
[2] INAF, Osservatorio Astrofisico di Arcetri, Largo E. Fermi 5, I-50125 Firenze, Italy
[3] National Radio Astronomy Observatory, [13] 1003 Lopezville Road, Socorro, NM 87801, USA
[4] Department of Physics, The University of Tokyo, Bunkyo-ku, Tokyo 113-0033, Japan
[5] The Institute of Physical and Chemical Research (RIKEN), 2-1, Hirosawa, Wako-shi, Saitama 351-0198, Japan
[6] Department of Astronomy, University of Virginia, Charlottesville, VA 22904, USA
[7] Max-Planck-Institut für extraterrestrische Physik (MPE), Giessenbachstrasse 1, D-85748 Garching, Germany
[8] Academia Sinica Institute of Astronomy and Astrophysics (ASIAA), No. 1, Section 4, Roosevelt Road, Taipei 10617, Taiwan
[9] Institut de Radioastronomie Millimétrique (IRAM), 300 rue de la Piscine, F-38400 Saint-Martin d'Hères, France
[10] Instituto de Radioastronomía y Astrofísica, Universidad Nacional Autónoma de México, Apartado 58090, Morelia, Michoacán, Mexico
[11] ESO, Karl Schwarzchild Str. 2, D-85478 Garching bei München, Germany
[12] Excellence Cluster Origins, Boltzmannstrasse 2, D-85748 Garching bei München, Germany
*Received 2022 June 2; revised 2022 July 29; accepted 2022 July 30; published 2022 August 12*

## Abstract

To understand the origin of the diversity observed in exoplanetary systems, it is crucial to characterize the early stages of their formation, represented by solar-type protostars. Likely, the gaseous chemical content of these objects directly depends on the composition of the dust-grain mantles formed before the collapse. Directly retrieving the ice mantle composition is challenging, but it can be done indirectly by observing the major components, such as $NH_3$ and $CH_3OH$ at centimeter wavelengths, once they are released into the gas phase during the warm protostellar stage. We observed several $CH_3OH$ and $NH_3$ lines toward three Class 0 protostars in NGC 1333 (IRAS 4A1, IRAS 4A2, and IRAS 4B), at high angular resolution (1″; ∼300 au) with the VLA interferometer at 24–26 GHz. Using a non-LTE LVG analysis, we derived a similar $NH_3/CH_3OH$ abundance ratio in the three protostars (⩽0.5, 0.015–0.5, and 0.003–0.3 for IRAS 4A1, 4A2, and 4B, respectively). Hence, we infer they were born from precollapse material with similar physical conditions. Comparing the observed abundance ratios with astrochemical model predictions, we constrained the dust temperature at the time of the mantle formation to be ∼17 K, which coincides with the average temperature of the southern NGC 1333 diffuse cloud. We suggest that a brutal event started the collapse that eventually formed IRAS 4A1, 4A2, and 4B, which, therefore, did not experience the usual prestellar core phase. This event could be the clash of a bubble with NGC 1333 South, which has previously been evoked in the literature.

*Unified Astronomy Thesaurus concepts:* Interstellar medium (847); Protostars (1302); Young stellar objects (1834); Astrochemistry (75); Star formation (1569); Observational astronomy (1145); Chemical abundances (224); Interstellar molecules (849)

## 1. Introduction

The thousands of exoplanets discovered so far (e.g., http://exoplanet.eu/) provide clear evidence of the incredible variety of planetary systems, different from each other and from our solar system. To understand the origin of such diversity, it is crucial to characterize the early stages of the formation of a planetary system. To study the diversity of these early stages, a powerful observational diagnostic tool is their chemical composition (Ceccarelli et al. 2007; Sakai & Yamamoto 2013). Indeed, the chemical complexity in star-forming regions starts at the very beginning of the process, during the precollapse phase. At this stage, icy mantles form on interstellar grains and grow rich in hydrogenated species. Then, during the warm (>100 K) protostellar phase, the ice mantle species are released in the gas-phase through ice mantle sublimation (Viti et al. 2004; Herbst & Van Dishoeck 2009; Caselli & Ceccarelli 2012; Ö berg & Bergin 2021). Therefore, the composition of the icy mantles is crucial in establishing the available gaseous chemical content that could explain the observed chemical diversity.

Infrared (IR) absorption observations toward solar-type protostars have shown that the icy mantle's major components are $H_2O$, CO, $CO_2$, $CH_4$, $NH_3$, and $CH_3OH$ (e.g., Boogert et al. 2015). However, these observations can only be obtained toward sources with enough bright IR continuum emission, making it very difficult to characterize the ice mantles of deeply embedded protostars, and even more of prestellar cores. Another possibility for studying the ice mantle chemical composition is to observe their major components once they are released into the gas phase during the warm protostellar phase (see, e.g., Whittet et al. 2011).

In this context, $NH_3$ and $CH_3OH$ are the best, if not the only, major components of the icy mantles that trace the hot central protostar with ground-based high-angular-resolution observations. Indeed, CO is confused with the surrounding cloud, $CO_2$

[13] The National Radio Astronomy Observatory is a facility of the National Science Foundation operated under cooperative agreement by Associated Universities, Inc.

and $CH_4$ do not have dipole moments, and $H_2O$ is hampered by the terrestrial atmosphere.

This indirect method relies on the knowledge of the species formation pathways and that they are efficiently released into the gas with the water-ice mantle. In this case, the formation paths of $NH_3$ and $CH_3OH$ are very well studied: They are mainly formed in the prestellar phase on the icy grain mantles through N and CO hydrogenation (Watanabe & Kouchi 2002; Rimola et al. 2014; Song & Kästner 2017; Jonusas et al. 2020) even if, for $NH_3$, a gas-phase contribution with a subsequent depletion cannot be excluded (e.g., Le Gal et al. 2014; Caselli et al. 2022; Pineda et al. 2022; see also Figure B1). In the following, we assume that the observed composition of the gas phase reflects that of the icy mantles, because the latter, and all the species within, sublimate during the hot corino phase when the dust temperature reaches the water sublimation temperature ($\geqslant$100 K). Once released in the gas phase, both methanol and ammonia undergo chemical reactions that can alter their abundances. However, the continuous infall of newly sublimated material ensures that the gas-phase abundance of these two species indeed reflects the one on the grain mantles.

Finally, the $NH_3/CH_3OH$ abundance ratio on the grain mantles depends only on the physical conditions of the material before the collapse, namely gas density, dust temperature, and ice mantle formation timescale. These parameters regulate, for example, the N and CO hydrogenation efficiency and their residence time on the mantles (e.g., Caselli et al. 1993; Taquet et al. 2012; Aikawa et al. 2020). These physical conditions can be different based on the dynamical history of the single object, which could be affected by external factors (e.g., cloud–cloud collisions, supernova explosions, etc.).

In this Letter, we investigate the icy mantle composition, through the relative abundance of $NH_3$ and $CH_3OH$, of three Class 0 protostars. We used the VLA interferometer to trace the inner 300 au at centimeter wavelengths, where the dust is more likely optically thin (see, e.g., Li et al. 2017; De Simone et al. 2020; Ko et al. 2020). We also used previous millimeter observations of methanol and its isotopologues (Taquet et al. 2015; Yang et al. 2021) to estimate the dust absorption contribution and to constrain the $CH_3OH$ column density in case of optically thick emission.

The three targeted sources are located in the southern filament of the Perseus/NGC 1333 region ($\sim$300 pc; Zucker et al. 2018): the protobinary system IRAS 4A, composed of IRAS 4A1 and IRAS 4A2 (hereafter 4A1 and 4A2) separated by 1.″8 ($\sim$540 au), and IRAS 4B (hereafter 4B) located $\sim$30″ southeast of 4A2. The three sources are known to be hot corinos[14] (Sakai et al. 2006; Bottinelli et al. 2007; Taquet et al. 2015; De Simone et al. 2017; López-Sepulcre et al. 2017; De Simone et al. 2020). Recently, observational evidence pointed out that this filament, where the three protostars lie, could have been shaped by the clash of an expanding bubble with NGC 1333 (Dhabal et al. 2019; De Simone et al. 2022). In particular, Dhabal et al. (2019) suggested that this clash could have been responsible for the formation of the protostars.

## 2. Observations and Results

We used VLA observations in *K* band (project ID: 18B-166) described in De Simone et al. (2020). In summary, we targeted 10 $CH_3OH$ and 5 $NH_3$ lines, with frequencies from 23.8 to 26.4 GHz and a large range of upper-level energies ($E_{up}$) (Table 1). They were associated with 13 spectral windows with $\sim$0.017 MHz ($\sim$0.2 km s$^{-1}$) spectral channels and 1″ angular resolution. The absolute flux calibration error is $\leqslant$15%.[15] Data reduction and cleaning process were performed using CASA[16] and data analysis and images using GILDAS.[17] The continuum is obtained by averaging line-free channels from all the spectral windows. We self-calibrated, in phase and amplitude, using the line-free continuum channels and applied the solutions to both the continuum and molecular lines (see De Simone et al. 2020). The continuum-subtracted cubes were smoothed to 1 km s$^{-1}$. They were cleaned using a manually corrected threshold mask for each channel and a multiscale deconvolution (scales = [0, 5, 15, 18, 25]) with natural weighting. The synthesized beams are in Table 1.

Figure 1 reports the $NH_3$ velocity-integrated map for the targeted protostars (4A1, 4A2, and 4B) and the $CH_3OH$ ones for 4B (the 4A1 and 4A2 ones are in De Simone et al. 2020), overlapped with the continuum emission. All the targeted lines are detected with a signal-to-noise ratio $\geqslant$ 5. The molecular emission peaks at the protostellar continuum position (coordinates in Table 1), and it is not resolved at the current angular resolution. However, the emission of $NH_3$ (and $CH_3OH$; De Simone et al. 2020) around 4A1 and 4A2 is well disentangled. The spectra of the targeted lines extracted at the protostar continuum peak are shown in Figure 2.

We derived the velocity-integrated line intensities for each transition using a Gaussian fit for $CH_3OH$, and a Hyperfine fit for $NH_3$, having spectrally resolved its hyperfine structure. The latter is assuming (i) the same excitation temperature and width for all the components, (ii) a Gaussian distribution of velocity, and (iii) nonoverlapping components. Then, the $NH_3$ integrated emission is computed as the sum of the integrated area of the main and the satellite hyperfine components. The fit results are reported in Table 1. The velocity peaks are consistent with the systemic velocity of the cloud hosting the protostars ($\sim$6.7 km s$^{-1}$).

In summary, we detected and imaged multiple lines of ammonia (from (3, 3) to (7, 7)) and methanol toward the hot corinos, 4A1, 4A2, and 4B, at compact scale ($\geqslant$300 au) around the central region.

## 3. Radiative Transfer and Astrochemical Modeling

### 3.1. Radiative Transfer Modeling

Having detected several lines of $NH_3$ and $CH_3OH$ covering a large range of $E_{up}$ (see Table 1) we performed a multiline analysis to derive their abundance ratio. More specifically, we used a non-LTE analysis via our in-home large velocity gradient (LVG) code `grelvg` (Ceccarelli et al. 2003) to predict the molecular line intensities that will be simultaneously fitted via comparison to the observed ones using a $\chi^2$ minimization.

The collisional coefficients of $CH_3OH$ and $NH_3$ with para-$H_2$ are from the BASECOL database (Dubernet et al. 2013). They are computed between 10 and 200 K by Rabli & Flower (2010) for the first 256 levels of A- and E-$CH_3OH$ and by Bouhafs et al. (2017) for the lowest 17 and 34 levels of ortho- and para-$NH_3$, respectively. We assumed a semi-infinite

[14] Hot corinos are compact (<100 au), hot ($\geqslant$100 K), and dense ($n_{H_2} \geqslant 10^7$ cm$^{-3}$) regions (e.g., Ceccarelli 2004) around solar-type protostars, enriched in interstellar complex organic molecules (iCOMs; Herbst & Van Dishoeck 2009; Ceccarelli et al. 2017).

[15] https://science.nrao.edu/facilities/vla/docs/manuals/oss/performance/fdscale

[16] https://casa.nrao.edu/

[17] http://www.iram.fr/IRAMFR/GILDAS

**Table 1**
Spectral Parameters, Synthesized Beams, and the Gaussian and Hyperfine fit Results for $CH_3OH$ and $NH_3$, Respectively, Extracted toward the Protostar's Continuum peak

| Transition | Frequency[a] (GHz) | $E_{up}$[a] (K) | log $A_{ij}$[a] | Synthesized Beam maj × min (PA) (″ × ″ (°)) | Source $\int T_B dV$ (K km s$^{-1}$) | Source $V_{peak}$[b] (km s$^{-1}$) | Source FWHM[b] (km s$^{-1}$) | rms (K) |
|---|---|---|---|---|---|---|---|---|
| | $CH_3OH$ | | | | | IRAS 4B $03^h29^m12^s.02$, 31°13′07.″9 | | |
| 3(2,1)–3(1,2) E | 24.9287 | 36 | −7.2 | 0.97 × 0.95 (−12) | 17(2) | +6.9(0.1) | 1.5(0.2) | 1.2 |
| 4(2,2)–4(1,3) E | 24.9334 | 45 | −7.1 | 0.97 × 0.95 (−12) | 21(3) | +6.9(0.2) | 2.2(0.4) | 1.2 |
| 2(2,0)–2(1,1) E | 24.9343 | 29 | −7.2 | 0.97 × 0.95 (−12) | 17(3) | +6.9(0.2) | 2.3(0.4) | 1.2 |
| 5(2,3)–5(1,4) E | 24.9590 | 57 | −7.1 | 0.97 × 0.95 (−12) | 17(2) | +6.8(0.1) | 1.5(0.2) | 1.2 |
| 6(2,4)–6(1,5) E | 25.0181 | 71 | −7.1 | 0.97 × 0.95 (−19) | 21(3) | +6.9(0.2) | 2.3(0.5) | 1.4 |
| 7(2,5)–7(1,6) E | 25.1248 | 87 | −7.1 | 0.98 × 0.95 (−21) | 19(2) | +6.8(0.1) | 1.7(0.2) | 1.5 |
| 8(2,6)–8(1,7) E | 25.2944 | 106 | −7.0 | 0.96 × 0.94 (−11) | 19(2) | +6.9(0.1) | 1.9(0.3) | 1.2 |
| 9(2,7)–9(1,8) E | 25.5414 | 127 | −7.0 | 0.96 × 0.92 (−50) | 22(3) | +6.8(0.1) | 1.8(0.3) | 1.4 |
| 10(2,8)–10(1,9) E | 25.8782 | 150 | −7.0 | 0.97 × 0.93 (−35) | 16(2) | +7.1(0.1) | 1.9(0.3) | 1.1 |
| 11(2,9)–11(1,10) E | 26.3131 | 175 | −6.9 | 0.94 × 0.91 (−35) | 14(2) | +6.6(0.2) | 1.4(0.5) | 1.4 |
| | $NH_3$ | | | | | IRAS 4B $03^h29^m12^s.02$, 31°13′07.″9 | | |
| (3,3) | 23.8701 | 124 | −6.6 | 1.00 × 0.95 (+6) | 64(8) | +7.2(0.2) | 1.7(0.5) | 1.5 |
| (4,4) | 24.1394 | 201 | −6.5 | 0.99 × 0.94 (−2) | 41(7) | +7.1(0.1) | 1.7(0.1) | 1.4 |
| (5,5) | 24.5329 | 296 | −6.5 | 0.99 × 0.95 (−3) | 39(7) | +6.6(0.4) | 2.5(0.7) | 1.4 |
| (6,6) | 25.0560 | 409 | −6.5 | 0.97 × 0.95 (−18) | 37(7) | +6.1(0.2) | 1.7(0.4) | 1.4 |
| (7,7) | 25.7151 | 639 | −6.4 | 0.96 × 0.92 (−45) | 27(7) | +6.9(0.3) | 1.7(0.1) | 1.4 |
| | $NH_3$ | | | | | IRAS 4A2 $03^h29^m10^s.43$, 31°13′32.″1 | | |
| (3,3) | 23.8701 | 124 | −6.6 | 1.00 × 0.95 (+6) | 169(20) | +6.9(0.1) | 2.3(0.1) | 1.3 |
| (4,4) | 24.1394 | 201 | −6.5 | 0.99 × 0.94 (−2) | 89(14) | +6.9(0.1) | 1.8(0.1) | 1.2 |
| (5,5) | 24.5329 | 296 | −6.5 | 0.99 × 0.95 (−3) | 54(14) | +6.9(0.1) | 1.7(0.2) | 1.2 |
| (6,6) | 25.0560 | 409 | −6.5 | 0.97 × 0.95 (−18) | 62(11) | +6.5(0.1) | 2.3(0.1) | 1.1 |
| (7,7) | 25.7151 | 639 | −6.4 | 0.96 × 0.92 (−45) | 40(8) | +7.1(0.1) | 1.8(0.1) | 1.0 |
| | $NH_3$ | | | | | IRAS 4A1 $03^h29^m10^s.536$, 31°13′31.″07 | | |
| (3,3) | 23.8701 | 124 | −6.6 | 1.00 × 0.95 (+6) | 121(16) | +6.4(0.1) | 2.7(0.2) | 1.3 |
| (4,4) | 24.1394 | 201 | −6.5 | 0.99 × 0.94 (−2) | 90(13) | +6.5(0.1) | 1.9(0.1) | 1.0 |
| (5,5) | 24.5329 | 296 | −6.5 | 0.99 × 0.95 (−3) | 87(12) | +6.4(0.1) | 2.5(0.1) | 1.0 |
| (6,6) | 25.0560 | 409 | −6.5 | 0.97 × 0.95 (−18) | 87(11) | +6.7(0.1) | 2.9(0.2) | 1.1 |
| (7,7) | 25.7151 | 639 | −6.4 | 0.96 × 0.92 (−45) | 46(9) | +6.4(0.1) | 1.9(0.2) | 1.1 |

**Notes.**
[a] Spectroscopic parameters are by Xu et al. (2008) from CDMS (Müller et al. 2005) for $CH_3OH$, and by Yu et al. (2010) from JPL Pickett et al. (1998) for $NH_3$.
[b] The spectral resolution is 1 km s$^{-1}$.

slab geometry to compute the line escape probability as a function of the line optical depth, the $H_2$ ortho-to-para ratio equal to 3, the $CH_3OH$ A-type/E-type ratio equal to 1, and the $NH_3$ ortho-to-para ratio equal to 2. The latter will be discussed and justified a posteriori in Section 4.

*Methodology*—A detailed description of the adopted methodology is in Appendix A, and a figurative scheme is shown in Figure A1. Here we summarize the major steps.

We first performed the LVG analysis of the VLA methanol lines at 25 GHz in order to constrain the gas density and temperature, and to derive the $CH_3OH$ column density and emitting size (the 4A1 and 4A2 ones have been derived in De Simone et al. 2020). All $CH_3OH$ transitions were optically thick so that the derived column density was only a lower limit. To constrain the $CH_3OH$ column density, we used the observations at millimeter wavelengths (from Taquet et al. 2015; Yang et al. 2021, for 4A2 and 4B, respectively, see Table 3) once corrected for the dust absorption factor (30% at 143 GHz for 4A2 and 50% at 243 GHz for 4B; see Appendix A). For 4A1 there are no methanol millimeter lines detected, so we report only a lower limit of its column density.

Then, assuming that $NH_3$ traces the same gas as $CH_3OH$,[18] namely assuming gas density and temperature ranges of $CH_3OH$, we performed the LVG analysis of the $NH_3$ lines to derive the $NH_3$ column density and the emitting size.

Finally, we computed the $NH_3/CH_3OH$ abundance ratio, using the column densities of $NH_3$ and $CH_3OH$ corresponding to the common derived source size. The derived ratio in 4A1 is an upper limit due to the unconstrained methanol column density. The derived values are $\leqslant$0.5, 0.015–0.5, and 0.003–0.3, for 4A1, 4A2, and 4B.

[18] This assumption is verified a posteriori as described in Appendix A.

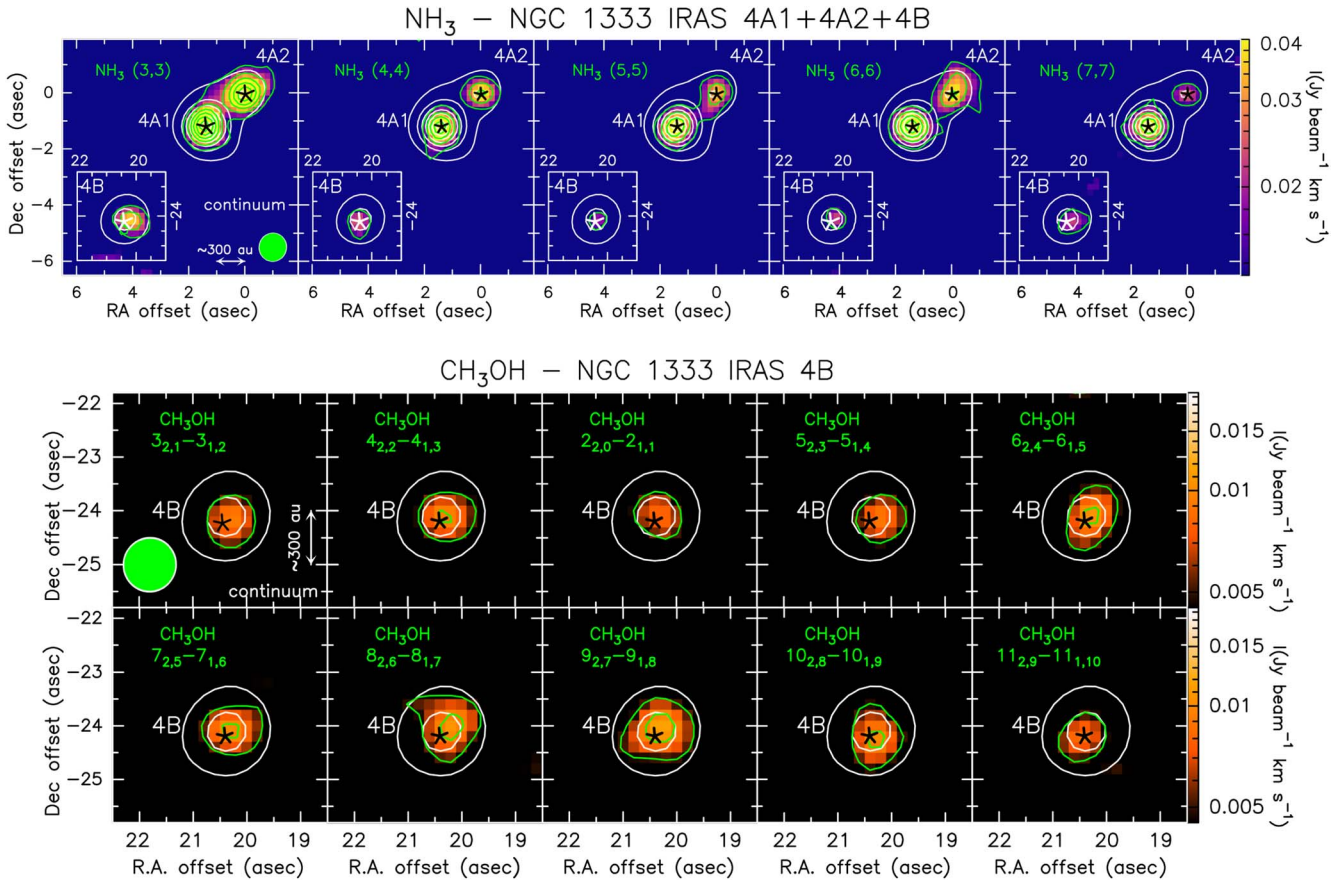


**Figure 1.** Top panels: $NH_3$ velocity-integrated maps (from $-30$ to $+45$ km s$^{-1}$ with respect to the $v_{sys}$ to include all the hyperfine components) toward IRAS 4A1, 4A2, and 4B in color scale starting from $3\sigma$, with green first contour and steps of $3\sigma$ ($\sigma = 4.4$ mJy beam$^{-1}$), overlapped with the continuum in white contours (from $50\sigma$ with steps of $100\sigma$). Bottom panels: $CH_3OH$ velocity-integrated maps toward IRAS 4B (from $-2$ to $+2$ km s$^{-1}$ with respect to the $v_{sys}$) in color scale starting from $3\sigma$, with green first contour and steps of $3\sigma$ ($\sigma = 1.6$ mJy beam$^{-1}$ km s$^{-1}$) overlapped with the continuum in white contours (from $50\sigma$ with steps of $100\sigma$). The $CH_3OH$ maps for 4A1 and 4A2 are reported in De Simone et al. (2020). The stars mark the protostar positions. Synthesized beams are in the lower corners.

The $1\sigma$ confidence level ranges of the LVG fitting results are reported in Table 2. As a result, both $CH_3OH$ and $NH_3$ are tracing compact (<100 au), dense (>$10^6$ cm$^{-3}$), and hot (>100 K) gas, fully consistent with the integrated emission maps (Figure 1) and the fact that we are observing the compact hot corino emission.

### 3.2. Astrochemical Modeling

The adopted model consists of two phases: (1) the mantle formation during the cold phase and (2) the sublimation of the water-rich mantles when the dust temperature reaches the water sublimation temperature. During the first phase, only a very small fraction (∼1%) of the frozen species is injected into the gas phase by nonthermal desorption mechanisms (Minissale et al. 2016), so this does not impact the amount of frozen species in the grain mantles before the second step occurs. During the second phase, the whole mantle sublimates so that the relative abundances observed in the gas phase reflect the composition of the mantles. Our modeling focuses on the first phase because the abundance on the grain mantles is the key point.

#### 3.2.1. Model Description

We used the astrochemical model GRAINOBLE (Taquet et al. 2012, 2013; Ceccarelli et al. 2018) to predict the evolution of the frozen $NH_3/CH_3OH$ abundance ratio as a function of the precollapse physical conditions (density, dust temperature, timescale).

Briefly, it is a time-dependent three-phase grain-gas chemistry code that computes the layered grain mantles structure. The gas-phase reaction network is an updated version of the KIDA 2014 network (https://kida.astrochem-tools.org/; Wakelam et al. 2015), with the reactions described in Tinacci et al. (2022a). The surface reactions are assumed to occur only in the last two formed mantle layers, the latter being in contact with the gas phase. In this work, we only considered the hydrogenation and oxidation of the species frozen on the grain mantle. In general, when the required information is available, we used the Eckart formalism to describe the probability for a reaction with an activation barrier to occur (Taquet et al. 2013). This is the case for the hydrogenation of CO into $H_2CO$ and $CH_3OH$ and the CO oxidation into $CO_2$. In addition, hydrogenation of O, $O_2$, and $O_3$ leads to water and of N to ammonia. On the other hand, C hydrogenation cannot occur, as carbon atoms chemically bind with the water molecules of the ice (e.g., Shimonishi et al. 2018). Methane is, therefore, formed by the hydrogenation of frozen CH. The binding energies used are those reported in Taquet et al. (2012), updated using the ones computed by Minissale et al. (2016), Song & Kastner (2016), Shimonishi et al. (2018), Ferrero et al. (2020), and Minissale et al. (2022). In particular, for CO, N, and $N_2$, we

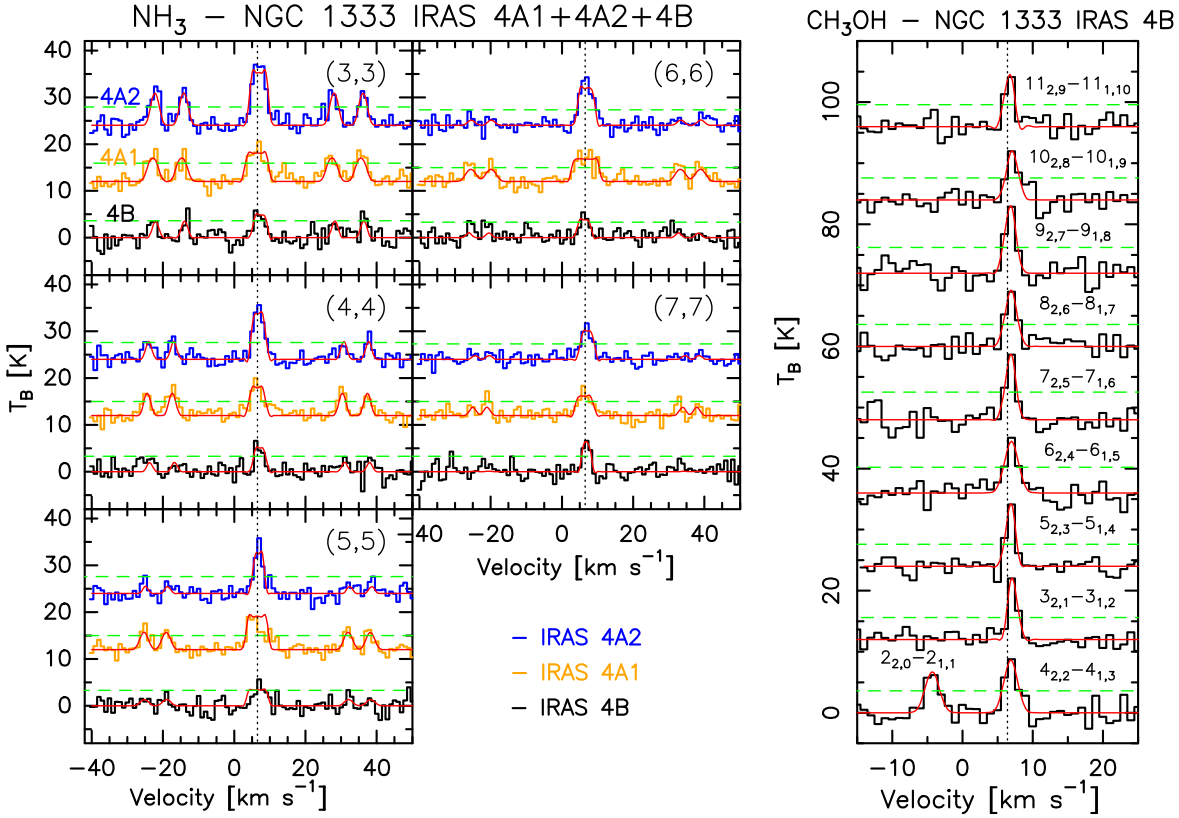


**Figure 2.** Left panels: $NH_3$ lines (marked in each panel) detected toward the continuum peak of IRAS 4B (black), 4A1 (orange), and 4A2 (blue). The red curves show the best hyperfine fits. Right panel: $CH_3OH$ lines (marked on each spectrum) detected in the VLA *K* band toward 4B. The red curves show the best Gaussian fits. In all panels, each spectrum is shifted by 12 K from the previous one, the vertical dotted black lines report the $v_{sys}$ (6.7 km $s^{-1}$), and the horizontal green dashed lines show the $3\sigma$ level.

**Table 2**
Results of the Non-LTE LVG Analysis of $CH_3OH$ and $NH_3$ toward IRAS 4A1, 4A2, and 4B Using the `grelvg` Code

| | | IRAS 4A1 | IRAS 4A2 | IRAS 4B |
|---|---|---|---|---|
| $n_{H_2}$ | ($cm^{-3}$) | $\geqslant 2 \times 10^6$ | $\geqslant 7 \times 10^6$ | $\geqslant 2 \times 10^6$ |
| $T_{kin}$ | (K) | 100–120 | 140–160 | 150–190 |
| $N_{CH_3OH}$ | ($cm^{-2}$) | $\geqslant 10^{19}$ | $(0.6–4) \times 10^{19}$ | $(1–8) \times 10^{19}$ |
| $N_{NH_3}$ | ($cm^{-2}$) | $(1–5) \times 10^{18}$ | $(0.6–3) \times 10^{18}$ | $(0.2–3) \times 10^{18}$ |
| size | ($''$) | 0.24–0.26 | 0.19–0.24 | 0.18–0.20 |
| $NH_3/CH_3OH$ | ··· | $\leqslant 0.5$ | 0.015–0.5 | 0.003–0.3 |

**Note.** The reported values are the $1\sigma$ confidence level.

assumed 1750, 720, and 1300 K, respectively. The diffusion to binding energy is assumed to be 0.5, following recent experimental and theoretical results (e.g., He et al. 2018).

We assumed that the $H_2$ number density $n_{H_2}$ of the molecular cloud is constant and an average grain radius of 0.1 $\mu$m, typical of the Galactic ISM grains. The gas and dust are assumed to be thermally coupled. To test that, we ran the model with the gas warmer than the dust. This scenario could be the result of an external shock, where there is a sudden increase in the gas temperature while the dust remains cool. Therefore, we assumed the gas temperature is as high as 100 K (typical temperature of shocked gas; e.g., Codella et al. 2017). The results are basically the same, so we will not discuss them in the following.

The initial elemental abundances were assumed to be the solar ones (Asplund et al. 2009) depleted following Jenkins (2009), where we assumed the most depleted cases: $O/H = 2.8 \times 10^{-4}$, $C/H = 1.7 \times 10^{-4}$, and $N/H = 5.3 \times 10^{-5}$.

We ran a grid of models with different $H_2$ densities, (0.1, 1, 10) $\times 10^5$ $cm^{-3}$, and temperatures, from 8 to 25 K. Each model starts with all the elements in atomic form except hydrogen, which is molecular, and the chemical composition is left to evolve for $10^7$ yr. Eventually, the formed mantle is constituted of approximately 100–160 layers, depending on the model parameters.

### 3.2.2. Model Results

We first verified that the steady-state mantle composition of the model with $n_{H_2} = 10^4$ $cm^{-3}$ and $T = 10$ K (a typical molecular cloud) is consistent with the observations of similar regions (Boogert et al. 2015): $H_2O/H_2 \sim 1 \times 10^{-4}$, $CO/H_2 \sim 3 \times 10^{-5}$, $CO_2/H_2 \sim 3 \times 10^{-5}$, $CH_3OH/H_2 \sim 4 \times 10^{-5}$, and $NH_3/H_2 \sim 2 \times 10^{-5}$. This good agreement encourages the reliability of the predictions obtained with different densities and temperatures.

Figure 3 reports the theoretical predictions of the frozen $NH_3/CH_3OH$ as a function of the precollapse dust temperature at different timescales and $H_2$ density.

*Time dependence*—The $NH_3/CH_3OH$ abundance ratio decreases with time until it reaches a constant value after about (1, 3, 10) $\times 10^5$ yr, with $H_2$ densities of (10, 1, 0.1) $\times 10^5$ $cm^{-3}$, respectively. This is because methanol forms after ammonia. First, when the N atoms land on the grain surfaces, they

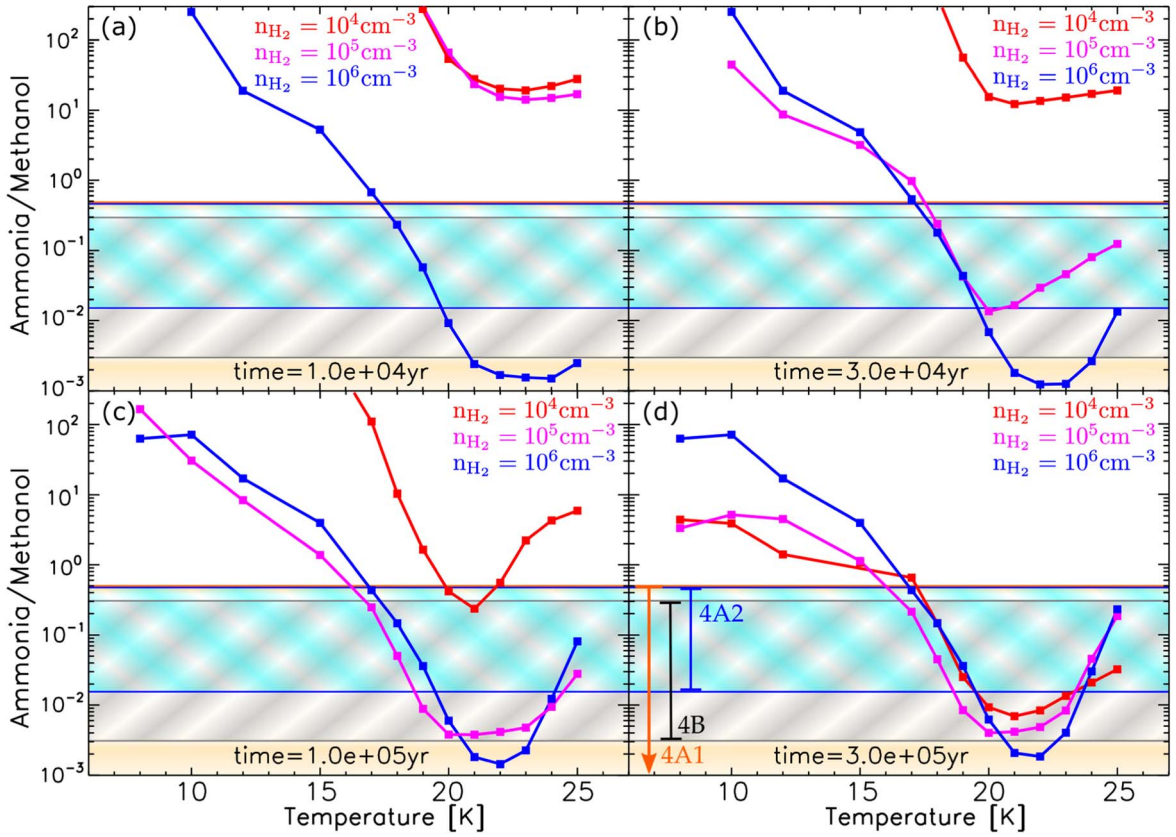


**Figure 3.** Theoretical predictions of $NH_3/CH_3OH$ abundance ratio vs. the precollapse dust temperature at different timescales (time = (0.1, 0.3, 1, 3)$10^5$ yr, in panels (a), (b), (c), and (d), respectively) and $H_2$ density ($n_{H_2}$ = (0.1, 1, 10)$10^5$ $cm^{-3}$, in red, magenta, and blue respectively), obtained with the GRAINOBLE code. Blue, gray, and orange bands represent the $NH_3/CH_3OH$ values derived from the LVG analysis in 4A2, 4B, and 4A1, respectively.

rapidly undergo hydrogenation, which is a barrierless process, while carbon is still atomic. Then, the gaseous abundance of N drops because nitrogen goes into $N_2$, and CO forms. Finally, once the gaseous CO freezes out into the mantles, methanol is formed by CO hydrogenation.

*Temperature dependence*—With the increase of the dust temperature, the residence time of N on the mantle decreases and, consequently, the ammonia abundance diminishes. On the contrary, the $CH_3OH$ abundance on the mantle remains roughly constant until about 25–30 K, at which temperatures CO sublimates from the grain surfaces. Therefore, the $NH_3/CH_3OH$ ratio decreases with increasing temperature. However, once the dust temperature becomes larger than the $N_2$ sublimation temperature (∼20 K), $N_2$ is released into the gas phase, where it can react in the gas phase to form gaseous $NH_3$ (e.g., Le Gal et al. 2014). Because the dust temperature is still low, the gaseous $NH_3$ immediately depletes onto the grain surface (see Figure B1), increasing again the $NH_3/CH_3OH$ ratio (see Figure 3).

*Density dependence*—Increasing $n_{H_2}$, the curves shift toward shorter times because of the higher accretion rate of the species in the mantle. Indeed, the three curves coincide at time larger than $\sim 3 \times 10^5$ yr (as shown in Figure 3).

## 4. Discussion

The first strong conclusion of the new observations is that the three protostars (4A1, 4A2, and 4B) possess a similar $NH_3/CH_3OH$ ratio (Figure 3), which points to similar precollapse conditions. This would be expected for IRAS 4A1 and 4A2, as they are coeval companions of a binary system. However, it is not obvious for IRAS 4B, which is located ∼30″ (∼9000 au) away from the binary system. In summary, the three protostars were born from precollapse material with similar physical conditions.

Additionally, the comparison between the observations and the theoretical model predictions provides the following two strong constrains on the precollapse: (1) A collapse timescale less than $\sim 10^4$ and $\sim 10^5$ yr for a density of $10^6$ and $10^4$ $cm^{-3}$, respectively, cannot reproduce the observed $NH_3/CH_3OH$ ratio; (2) the precollapse dust temperature has to be larger than 17 K in all the three protostars. In other words, the grain mantles of the three protostars was formed during a period not smaller than $\sim 10^4$–$10^5$ yr, depending on the cloud density.

Most importantly, the dust was relatively warm, about 17 K. We emphasize that this dust is the one corresponding to the inner <100 au of the hypothetical condensations from which the three protostars were born. If we consider the typical temperature of a prestellar core at this scale, we would expect much lower temperatures, around 7 K (as for the prototypical prestellar core L1544; Crapsi et al. 2007). Therefore, the results of 17 K is apparently puzzling. On the other hand, the large-scale maps of Herschel–Planck (Zari et al. 2016) show that the average dust temperature of the south part of NGC 1333 is around 17 K, with the denser parts at 14–15 K (Zhang et al. 2022). Probably the only way to reconcile this ensemble of information is that the three protostars actually did not have the usual dense and cold precollapse phase period, as their mantles were mostly built during a relatively warm phase (dust temperature ∼17 K), which is characteristic of the less dense

cloud material in NGC 1333 South. In other words, something must have happened that suddenly compressed the gas and triggered a fast collapse and the protostars' formation.

It is well known that the NGC 1333 region is heavily shaped by external triggers. In particular, it has been suggested that the filament where the three protostars lie could have been shaped by a colliding turbulent cell that would have triggered the birth of the protostars (Dhabal et al. 2019). The recent detection of a train of finger-shaped shocked SiO-emitting gas around IRAS 4A supports that an expanding bubble clashed against the southern part of NGC 1333 (De Simone et al. 2022). Our new analysis adds a new element to the story: The clash has brutally started the collapse in a region where otherwise no precollapse cores existed.

Finally, the derived dust temperature at the time of the mantle formation, around 17 K, justifies a posteriori our choice of a $NH_3$ ortho-to-para ratio equal to 2. This value corresponds to the thermal equilibrium at 15 K (e.g., Faure et al. 2013) and applies if ammonia was mostly formed on the icy grain surfaces. We emphasize that the results of the analysis would not significantly change if a ratio equal to 1 (appropriate for larger temperatures) is adopted.

## 5. Conclusions

We observed $NH_3$ and $CH_3OH$ lines at centimeter wavelengths with the VLA, toward the NGC 1333 IRAS 4A1, 4A2, and 4B protostars, finding that they are tracing the compact (<100 au) hot corino region. Using a non-LTE analysis we derived similar $NH_3/CH_3OH$ abundance ratios for all three protostars ($\leqslant$0.5 for IRAS 4A1, 0.015–0.5 for IRAS 4A2, and 0.003–0.3 for IRAS 4B). This means that they were born from precollapse material with similar physical conditions.

Comparing the observed ratio with astrochemical models we constrained the precollapse conditions, finding that the dust was particularly warm ($\geqslant$17 K). In other words, the protostellar ice mantles were mostly formed during a warm phase that it is typical of the less dense material of NGC 1333 southern region. We conclude that the collapse could have been brutally started by the clash of an external bubble with NGC 1333 in a warm region where no precollapse core existed.

Finally, these results advance the study of the chemical and dynamical history of protostars and open the way to future projects with the upcoming centimeter facilities such as ngVLA[19] and SKA.[20] Additionally, the synergy between the upcoming centimeter facilities and the infrared ones (e.g., JWST[21] and ELT,[22] which will provide the ice mantle composition along the line of sight of protostars and protoplanetary disks) will be crucial for characterizing the chemical and physical evolution of the early stages of planetary system formation.

This work has received funding from the European Research Council (ERC) under the European Union's Horizon 2020 research and innovation program, for the Project "The Dawn of Organic Chemistry" (DOC), grant agreement No. 741002. H.B. L. is supported by the Ministry of Science and Technology (MoST) of Taiwan (grant Nos. 108-2112-M-001-002-MY3 and 110-2112-M-001-069-).

[19] https://ngvla.nrao.edu/
[20] https://www.skatelescope.org/
[21] https://www.jwst.nasa.gov/
[22] https://elt.eso.org/

## Appendix A
## $NH_3$ and $CH_3OH$ Line Analysis

Figure A1 shows the scheme of the $CH_3OH$ and $NH_3$ line analysis performed to compute the $NH_3/CH_3OH$ abundance ratio in the three protostars. All the computations and predictions of column density, temperature, density and size are performed with a non-LTE LVG method (Ceccarelli et al. 2003) with the following strategy:

*Methanol line analysis*—The methanol line analysis for 4A1 and 4A2 is reported in De Simone et al. (2020). We carried out a similar analysis for 4B. We ran a large grid of models (~70,000) covering the frequency of the observed $CH_3OH$ lines, a total (A-type plus E-type) column density $N_{CH_3OH}$ from $2 \times 10^{16}$ to $16 \times 10^{19}$ cm$^{-2}$, a gas density $n_{H_2}$ from $10^6$ to $10^9$ cm$^{-3}$, both sampled in logarithmic scale, and a temperature $T$ from 40 to 200 K, sampled in linear scale. We simultaneously fit the measured $CH_3OH$ line intensities, for 4B, via comparison with those simulated by the LVG model, leaving $N_{CH_3OH}$, $n_{H_2}$, $T$, and the emitting size $\theta$ as free parameters. Following the observations, we assumed a line width equal to 2 km s$^{-1}$, and we included the calibration uncertainty (15%) in the observed intensities. Solutions with $N_{CH_3OH} \geqslant 10^{18}$ cm$^{-2}$ are within $1\sigma$ of the confidence level, emitted by a source of 0.″18–0.″40. The reduced $\chi^2$ ($\chi^2_R$, defined as the $\chi^2$ per degree of freedom) decreases, increasing the $CH_3OH$ column density, until a constant value ($\chi^2_R$~0.7), as all the observed lines become optically thick ($\tau = 1.5$–4) and, consequently, the emission is that of a blackbody.

*Constrain methanol column density*—For all three sources, all the methanol lines observed at 25 GHz are optically thick so that we could derive only a lower limit for the methanol column density. To constrain the methanol column density, we used its isotopologues observed at millimeter wavelengths, once corrected for the absorption factor due to the dust.

While for 4A1 there are no methanol lines detected at millimeter wavelengths, for 4A2 there are several detected lines of $CH_3OH$ and $^{13}CH_3OH$ at 143 GHz by Taquet et al. (2015), and for 4B there are three detected $CH_3OH$ and one $CH_3^{18}OH$ line at 243 GHz by Yang et al. (2021)[23] (see Table A1). Note that the angular resolution of the millimeter observations are slightly different from our cm observations. We took that into account in the computation of the filling factor when performing the LVG analysis.

As explained in De Simone et al. (2020), we retrieved the correction factor due to the dust contribution as follows: (i) We predicted the methanol intensities at millimeter wavelengths using the gas conditions derived at centimeter wavelengthhs with the VLA methanol lines; (ii) we compared the predicted methanol millimeter line intensities with the observed ones; and (iii) we derived the dust optical depth at millimeter wavelength using Equation (1) in De Simone et al. (2020), and consequently the dust absorption factor. We found an absorption of 30% at 143 GHz for 4A2 and of 50% at 243 GHz for 4B.

We then corrected the integrated line intensities of the detected methanol isotopologues ($^{13}CH_3OH$ lines at 143 GHz for 4A2, and $CH_3^{18}OH$ line at 243 GHz for 4B) by the derived dust absorption factor, and we run again the LVG code including the isotopologues together with the methanol lines at

[23] Please note that we could not use the lines at 243 GHz by Yang et al. (2021) for 4A2 as the methanol lines where contaminated by the outflow and we could not derive a reliable dust absorption factor.

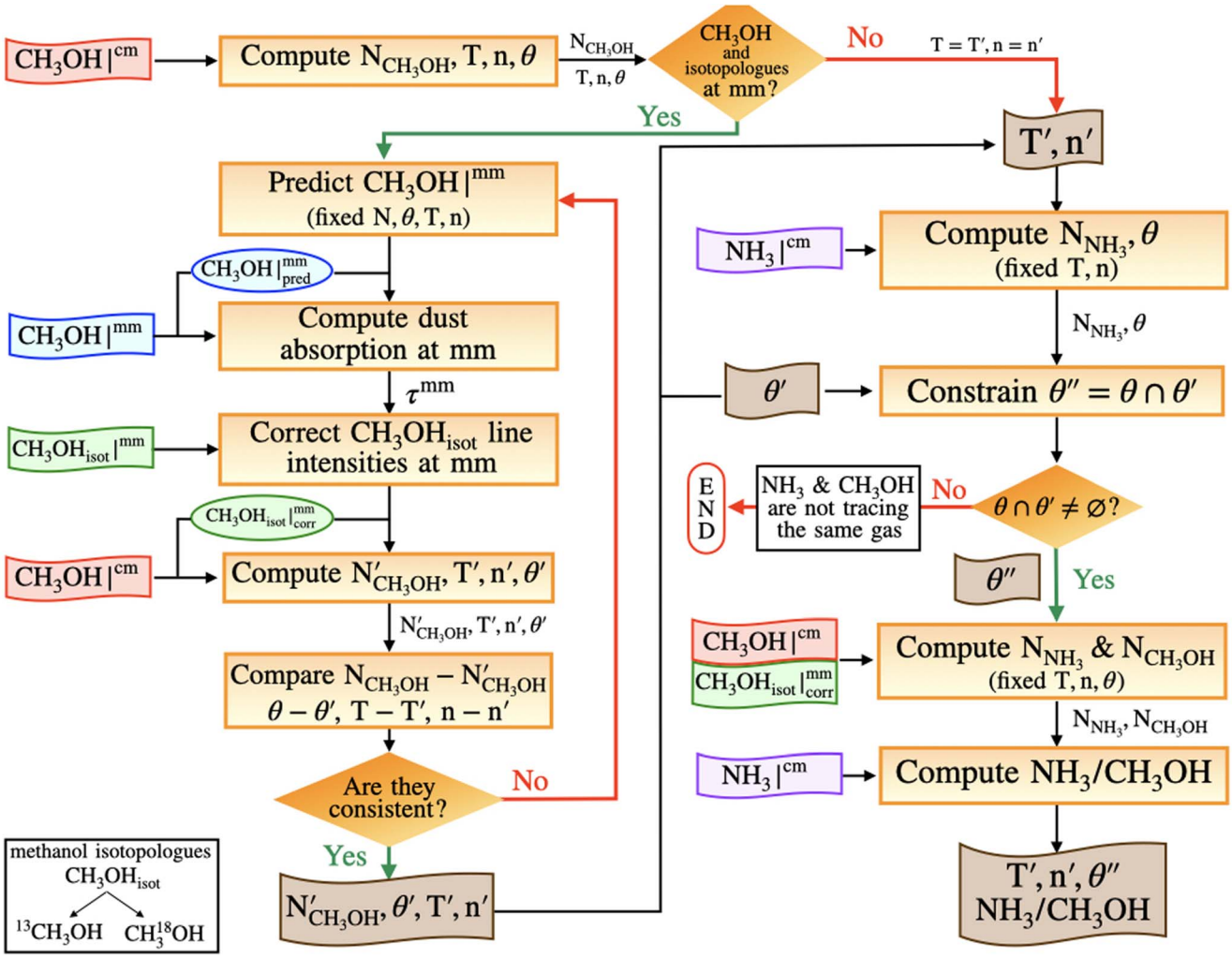


**Figure A1.** Scheme of the $CH_3OH$ and $NH_3$ line analysis performed to compute the $NH_3/CH_3OH$ abundance ratio in the three protostars. The $CH_3OH$ lines at centimeter wavelengths (red flag) are the ones observed at 25 GHz with the VLA (this work). The $CH_3OH$ lines at millimeter wavelengths (blue flag) and its isotopologues $CH_3OH_{isot}$ (green flag) are from Taquet et al. (2015) for 4A2 using $CH_3OH_{isot} = {}^{13}CH_3OH$, and from Yang et al. (2021) for 4B using $CH_3OH_{isot} = CH_3{}^{18}OH$. For 4A1 we do not have millimeter methanol detections. All the computations and predictions of column density N, temperature T, density $n$, and size $\theta$ are performed with a non-LTE LVG method.

25 GHz. We assumed a $^{12}C/^{13}C$ of ∼70 (Milam et al. 2005) and $^{16}O/^{18}O \sim 560$ (Wilson & Rood 1994). Because the $^{13}CH_3OH$ and $CH_3{}^{18}OH$ lines are optically thin, we could constrain the column density of methanol for 4A2 and 4B, finding 0.6–4 × $10^{19}$ cm$^{-2}$ and 1–8 × $10^{19}$ cm$^{-2}$, respectively. The gas density and temperature, the $CH_3OH$ column density, and emitting size for IRAS 4A1, 4A2, and 4B are reported in Table 2.

*Ammonia line analysis*—We then considered the source size, the gas density, and temperature ranges derived for methanol and ran a grid of models (∼5000) with these parameters to fit the observed ammonia lines for the three protostars, leaving the ammonia column density as a free parameter.

Following the observations, we assumed a line width of 12, 10, and 9 km s$^{-1}$ for 4A1, 4A2, and 4B, respectively, computed as the one derived from the hyperfine fitting (Table 1) multiplied by the number of components (main plus satellites). This is because we considered, in the LVG analysis only the rotational level of $NH_3$ for which we have collisional coefficients. The best fit is obtained for $N_{NH_3} = 2 \times 10^{18}$ cm$^{-2}$ with $\chi^2_R = 0.5$ for 4A1, $2 \times 10^{18}$ cm$^{-2}$ with $\chi^2_R = 1.1$ for 4A2, and $6 \times 10^{17}$ cm$^{-2}$ with $\chi^2_R = 0.8$ for 4B. The 1$\sigma$ confidence level range is reported in Table 2. The $NH_3$ (3,3) transition is often quite optically thick (∼20), while the others have opacity between 0.4 and 7. The (7,7) transition is always optically thin ($\leqslant$1), so it allowed us to constrain the $NH_3$ column density.

Please note that we also run the LVG model on the $NH_3$ alone, leaving the column density, temperature, density, and source size as free parameters. We compared the ammonia parameter space with that derived from the methanol analysis: The two parameter spaces overlap with the one of methanol being better constrained. Therefore, we proceeded as described above.

*Abundance ratios*—Finally, we computed the $NH_3/CH_3OH$ abundance ratio, using the column densities of $NH_3$ and $CH_3OH$ corresponding to the common source size derived from the LVG analysis described above.

The assumption that the two species are tracing the same gas is supported by the emission maps (Figure 1) and by the fact that a common source size has consistently been derived.

**Table A1**
Spectral parameters, Synthesized Beams, and Integrated Flux for $CH_3OH$, $^{13}CH_3OH$, and $CH_3^{18}OH$ Transitions at Millimeter Wavelengths toward IRAS 4A2 and IRAS 4B from Taquet et al. (2015) and Yang et al. (2021)

| Transition | Frequency[a] (GHz) | $E_{up}^{(a)}$ (K) | log $A_{ij}^{(a)}$ | Synthesized Beam maj×min (PA) ($'' \times ''(°)$) | $\int T_B dV$ (K km s$^{-1}$) |
|---|---|---|---|---|---|
| IRAS 4A2 (Taquet et al. 2015) | | | | | |
| $CH_3OH$ | | | | | |
| 3(1,3)–2(1,2) A | 143.8658 | 28 | −5.0 | 2.2 × 1.8(+25) | 6.5(1.5) |
| 7(3,5)–8(2,7) E | 143.1695 | 113 | −5.4 | 2.3 × 1.8(+26) | 3.6(1.2) |
| $^{13}CH_3OH$ | | | | | |
| 3(0,3)–2(0,2) A | 141.6037 | 14 | −4.9 | 2.1 × 1.7(+26) | 1.7(0.5) |
| 3(1,2)–2(1,1) A | 142.8077 | 28 | 4.9 | 2.1 × 1.7(+26) | 1.2(0.3) |
| 6(2,5)7(1,6) A | 142.8967 | 85 | −5.3 | 2.1 × 1.7(+26) | 1.5(0.5) |
| 7(0,7)–6(1,5) E | 163.8729 | 76 | −5.0 | 2.4 × 1.8(+114) | 1.4(0.4) |
| 6(2,4)–7(1,7) A | 165.2805 | 85 | −5.1 | 2.4 × 1.8(+114) | 0.8(0.2) |
| 13(1,12)–12(2,11) A | 165.2805 | 222 | −5.0 | 2.4 × 1.8(+114) | 1.3(0.4) |
| 2(1,1)–2(0,2) E | 165.5756 | 28 | −4.6 | 2.4 × 1.8(+114) | 1.8(0.4) |
| 3(1,2)–3(0,3) E | 165.6094 | 35 | −4.6 | 2.4 × 1.8(+114) | 2.0(0.4) |
| 4(1,3)–4(0,4) E | 165.6909 | 44 | −4.6 | 2.4 × 1.8(+114) | 1.8(0.4) |
| 5(1,4)–5(0,5) E | 165.3693 | 55 | −4.6 | 2.4 × 1.8(+114) | 1.8(0.4) |
| 6(1,5)–6(0,6) E | 166.1287 | 69 | −4.6 | 2.4 × 1.8(+114) | 1.8(0.4) |
| 7(1,6)–7(0,7) E | 166.5694 | 85 | −4.6 | 2.4 × 1.8(+114) | 2.4(0.5) |
| IRAS 4B (Yang et al. 2021) | | | | | |
| $CH_3OH$ | | | | | |
| 5(1,4)–4(1,3) A | 243.91579 | 50 | −4.2 | 0.6 × 0.4(0) | 21(2) |
| $CH_3^{18}OH$ | | | | | |
| 11(2,10)–10(3,7) A | 246.2566 | 184 | −4.6 | 0.6 × 0.4(0) | 6.0(1.6) |

Additionally, there is no theoretical reason for why they would trace different gas on these size scales, as they are released together into the gas phase once the ice mantles are sublimated. The obtained $NH_3/CH_3OH$ values are $\leqslant$0.5, 0.015–0.5, and 0.003–0.3 , for 4A1, 4A2 and 4B (Table 2). Note that for 4A1 we could derive only an upper limit for the ratio, because we could not constrain the methanol column density for the lack of methanol emission at millimeter wavelengths.

## Appendix B
## $NH_3$ Formation

Figure B1 (from Tinacci et al. 2022b) shows the interplay between the gas phase and the grain surface chemistry for the $NH_3$ formation. The major $NH_3$ formation path is through the hydrogenation of frozen N on the grain surfaces (Jonusas et al. 2020), as it is a fast and barrierless process. When the dust temperature is high enough to release $N_2$ into the gas phase for thermal desorption, the gas-phase pathway to form $NH_3$ takes place (Le Gal et al. 2014). However, the temperature is still low (around 20–25 K) for $NH_3$ to remain in the gas phase, therefore, it freezes out onto the grain. Once on the grain surface, $NH_3$ can be thermally desorbed or injected into the gas phase via the so-called chemical desorption (CD). While CD injects a small fraction ($\leqslant$1%) of the $NH_3$ into the gas phase, the thermal desorption, governed by the $NH_3$ The binding energy (BE) involves the whole frozen $NH_3$ (Minissale et al. 2016). In our case, $NH_3$ will be released into the gas phase through the sublimation of the icy mantles when the dust temperature reaches the water sublimation temperature (above 100 K).

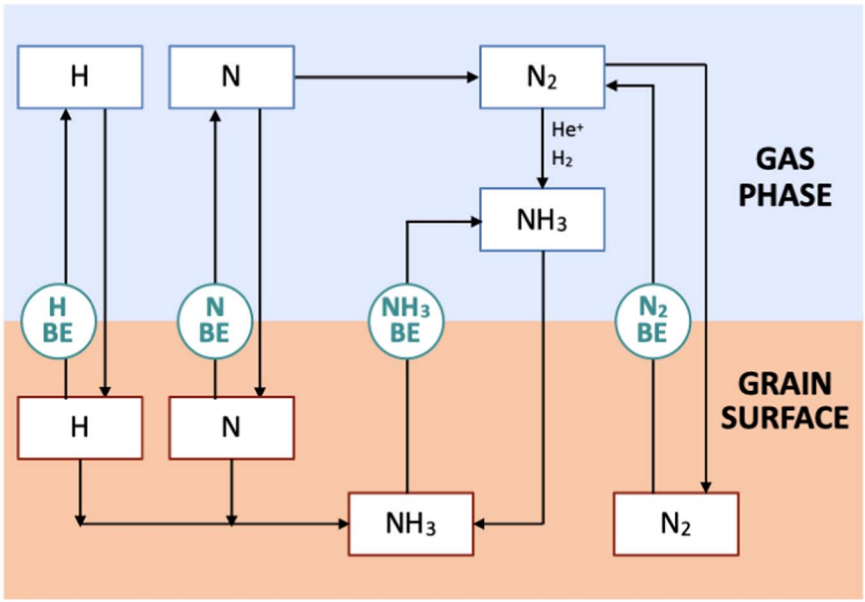


**Figure B1.** Scheme of the interplay between the gas phase and grain surface chemistry for the $NH_3$ formation (adapted from Tinacci et al. 2022b). The release of H, N, $N_2$, and $NH_3$ into the gas phase is regulated by their respective binding energies. BE stands for binding energy.

## ORCID iDs

Marta De Simone https://orcid.org/0000-0001-5659-0140
Cecilia Ceccarelli https://orcid.org/0000-0001-9664-6292
Claudio Codella https://orcid.org/0000-0003-1514-3074
Brian E. Svoboda https://orcid.org/0000-0002-8502-6431
Claire J. Chandler https://orcid.org/0000-0002-7570-5596
Mathilde Bouvier https://orcid.org/0000-0003-0167-0746
Satoshi Yamamoto https://orcid.org/0000-0002-9865-0970
Nami Sakai https://orcid.org/0000-0002-3297-4497
Yao-Lun Yang https://orcid.org/0000-0001-8227-2816
Paola Caselli https://orcid.org/0000-0003-1481-7911
Bertrand Lefloch https://orcid.org/0000-0002-9397-3826
Hauyu Baobab Liu https://orcid.org/0000-0003-2300-2626
Ana López-Sepulcre https://orcid.org/0000-0002-6729-3640
Laurent Loinard https://orcid.org/0000-0002-5635-3345
Jaime E. Pineda https://orcid.org/0000-0002-3972-1978
Leonardo Testi https://orcid.org/0000-0003-1859-3070

## References

Aikawa, Y., Furuya, K., Yamamoto, S., & Sakai, N. 2020, ApJ, 897, 110
Asplund, M., Grevesse, N., Sauval, A. J., & Scott, P. 2009, ARA&A, 47, 481
Boogert, A. C. A., Gerakines, P. A., & Whittet, D. C. B. 2015, ARA&A, 53, 541
Bottinelli, S., Ceccarelli, C., Williams, J. P., & Lefloch, B. 2007, A&A, 463, 601
Bouhafs, N., Rist, C., Daniel, F., et al. 2017, MNRAS, 470, 2204
Caselli, P., & Ceccarelli, C. 2012, A&ARv, 20, 56
Caselli, P., Hasegawa, T. I., & Herbst, E. 1993, ApJ, 408, 548
Caselli, P., Pineda, J. E., Sipilä, O., et al. 2022, ApJ, 929, 13
Ceccarelli, C. 2004, ASPC, 323, 195
Ceccarelli, C., Caselli, P., Fontani, F., et al. 2017, ApJ, 850, 176
Ceccarelli, C., Caselli, P., Herbst, E., Tielens, A. G. G. M., & Caux, E. 2007, in Protostars and Planets V, ed. B. Reipurth, D. Jewitt, & K. Keil (Tucson, AZ: Univ. Arizona Press), 47
Ceccarelli, C., Maret, S., Tielens, A. G. G. M., Castets, A., & Caux, E. 2003, A&A, 410, 587
Ceccarelli, C., Viti, S., Balucani, N., & Taquet, V. 2018, MNRAS, 476, 1371
Codella, C., Ceccarelli, C., Caselli, P., et al. 2017, A&A, 605, L3
Crapsi, A., Caselli, P., Walmsley, M. C., & Tafalla, M. 2007, A&A, 470, 221
De Simone, M., Ceccarelli, C., Codella, C., et al. 2020, ApJL, 896, L3
De Simone, M., Codella, C., Ceccarelli, C., et al. 2022, MNRAS, 512, 5214
De Simone, M., Codella, C., Testi, L., et al. 2017, A&A, 599, A121
Dhabal, A., Mundy, L. G., Chen, C.-y., Teuben, P., & Storm, S. 2019, ApJ, 876, 108
Dubernet, M.-L., Alexander, M. H., Ba, Y. A., et al. 2013, A&A, 553, A50
Faure, A., Hily-Blant, P., Le Gal, R., Rist, C., & Pineau des Forêts, G. 2013, ApJL, 770, L2
Ferrero, S., Zamirri, L., Ceccarelli, C., et al. 2020, ApJ, 904, 11
He, J., Emtiaz, S., & Vidali, G. 2018, ApJ, 863, 156
Herbst, E., & Van Dishoeck, E. 2009, ARA&A, 47, 427
Jenkins, E. B. 2009, ApJ, 700, 1299
Jonusas, M., Leroux, K., & Krim, L. 2020, JMoSt, 1220, 128736
Ko, C.-L., Liu, H. B., Lai, S.-P., et al. 2020, ApJ, 889, 172
Le Gal, R., Hily-Blant, P., Faure, A., et al. 2014, A&A, 562, A83
Li, J. I.-H., Liu, H. B., Hasegawa, Y., & Hirano, N. 2017, ApJ, 840, 72
López-Sepulcre, A., Sakai, N., Neri, R., et al. 2017, A&A, 606, A121
Milam, S. N., Savage, C., Brewster, M. A., Ziurys, L. M., & Wyckoff, S. 2005, ApJ, 634, 1126
Minissale, M., Aikawa, Y., Bergin, E., et al. 2022, ESC, 6, 597
Minissale, M., Dulieu, F., Cazaux, S., & Hocuk, S. 2016, A&A, 585, A24
Müller, H. S. P., Schlöder, F., Stutzki, J., & Winnewisser, G. 2005, JMoSt, 742, 215
Ö berg, K., & Bergin, E. A. 2021, PhR, 893, 1
Pickett, H. M., Poynter, R. L., Cohen, E. A., et al. 1998, JQSRT, 60, 883
Pineda, J. E., Harju, J., Caselli, P., et al. 2022, AJ, 163, 294
Rabli, D., & Flower, D. R. 2010, MNRAS, 406, 95
Rimola, A., Taquet, V., Ugliengo, P., Balucani, N., & Ceccarelli, C. 2014, A&A, 572, A70
Sakai, N., Sakai, T., & Yamamoto, S. 2006, PASJ, 58, L15
Sakai, N., & Yamamoto, S. 2013, ChRv, 113, 8981
Shimonishi, T., Nakatani, N., Furuya, K., & Hama, T. 2018, ApJ, 855, 27
Song, L., & Kastner, J. 2016, PCCP, 18, 29278
Song, L., & Kästner, J. 2017, ApJ, 850, 118
Taquet, V., Ceccarelli, C., & Kahane, C. 2012, A&A, 538, A42
Taquet, V., López-Sepulcre, A., Ceccarelli, C., et al. 2015, ApJ, 804, 81
Taquet, V., Peters, P. S., Kahane, C., et al. 2013, A&A, 550, A127
Tinacci, L., Ferrada-Chamorro, S., Ceccarelli, C., et al. 2022a, ApJS, 35 submitted
Tinacci, L., Germain, A., Pantaleone, S., et al. 2022b, ECS, 6, 1514
Viti, S., Collings, M. P., Dever, J. W., McCoustra, M. R. S., & Williams, D. A. 2004, MNRAS, 354, 1141

Wakelam, V., Loison, J. C., Herbst, E., et al. 2015, ApJS, 217, 20
Watanabe, N., & Kouchi, A. 2002, ApJL, 571, L173
Whittet, D. C. B., Cook, A. M., Herbst, E., Chiar, J. E., & Shenoy, S. S. 2011, ApJ, 742, 28
Wilson, T. L., & Rood, R. 1994, ARA&A, 32, 191
Xu, L.-H., Fisher, J., Lees, R., et al. 2008, JMoSp, 251, 305
Yang, Y.-L., Sakai, N., Zhang, Y., et al. 2021, ApJ, 910, 20
Yu, S., Pearson, J. C., Drouin, B. J., et al. 2010, JChPh, 133, 174317
Zari, E., Lombardi, M., Alves, J., Lada, C. J., & Bouy, H. 2016, A&A, 587, A106
Zhang, C., Zhang, G.-Y., Li, J.-Z., & Li, X.-M. 2022, RAA, 22, 055012
Zucker, C., Schlafly, E. F., Speagle, J. S., et al. 2018, ApJ, 869, 83